Wireless Frequency-Multiplexed Acoustic Array-based Acoustofluidics

Jiali Li†, Luyu Bo†, Teng Li, Penghui Zhao, Yingshan Du, Bowen Cai, Liang Shen, Wujin Sun, Wei Zhou*, Zhenhua Tian**

Jiali Li, Luyu Bo, Teng Li, Bowen Cai, Liang Shen, Prof. Zhenhua Tian
Department of Mechanical Engineering,
Virginia Polytechnic Institute and State University, Blacksburg, VA, 24060, USA
E-mail: tianz@vt.edu (Z.T.)

Penghui Zhao, Prof. Wujin Sun
Department of Biological System Engineering,
Virginia Polytechnic Institute and State University, Blacksburg, VA, 24060, USA

Yingshan Du
Department of Biomedical Engineering and Science,
Virginia Polytechnic Institute and State University, Blacksburg, VA, 24060, USA

Prof. Wei Zhou
Bradley Department of Electrical and Computer Engineering,
Virginia Polytechnic Institute and State University, Blacksburg, VA, 24060, USA

[†] J.L. and L.B. contributed equally to this work.
[*] Correspondence to: sunw@vt.edu (W.S.), wzh@vt.edu (W.Z.), tianz@vt.edu (Z.T.)

Keywords: Acoustofluidics, frequency-multiplexed acoustic array, acoustic patterning, laser Doppler vibrometry

Abstract

Acoustofluidics has shown great potential in enabling on-chip technologies for driving liquid flows and manipulating particles and cells for engineering, chemical, and biomedical applications. To introduce on-demand liquid sample processing and micro/nano-object manipulation functions to wearable and embeddable electronics, wireless acoustofluidic chips are highly desired. This paper presents wireless acoustofluidic chips to generate acoustic waves carrying sufficient energy and achieve key acoustofluidic functions, including arranging particles and cells, generating fluid streaming, and enriching in-droplet particles. To enable these functions, our wireless acoustofluidic chips leverage mechanisms, including inductive coupling-based wireless power transfer (WPT), frequency multiplexing-based control of multiple acoustic waves, and the resultant acoustic radiation and drag forces. For validation, the wirelessly generated acoustic waves are measured using laser vibrometry when different materials (*e.g.*, bone, tissue, and hand) are inserted between the WPT transmitter and receiver. Moreover, our wireless acoustofluidic chips successfully arrange nanoparticles into different patterns, align cells into parallel pearl chains, generate streaming, and enrich in-droplet microparticles. We anticipate this research to facilitate the development of embeddable wireless on-chip flow generators, wearable sensors with liquid sample processing functions, and implantable devices with flow generation and acoustic stimulation abilities for engineering, veterinary, and biomedical applications.

1. Introduction

Acoustofluidics, which fuses acoustics and fluid mechanics, use acoustic waves to generate fluid flow, as well as apply forces on small objects in fluids for contactless multifunctional object manipulation.[1–5] In recent year, acoustofluidics has been attracting increasing interest in the fields of engineering, biology, medicine, and chemistry,[6–11] as it enables various on-chip technologies, which can drive and control fluid flows for pumping,[12–14] mixing,[15,16] vortex generation,[17–19] *etc*., as well as achieve contactless, precise manipulation of nano-to-millimeter scale objects (*e.g.*, plasmids,[20,21] exosomes,[22] cells,[23–27] worms,[28] zebrafish,[29] and micro/nanoparticles[30–32]) in multiple modes such as arranging particle/cell distributions,[6,33] transporting cells,[34] separating cells,[35,36] controlling cell-cell distances,[37,38] isolating exosomes,[39,40] as well as rotating cells,[41] worms,[42,43] and zebrafish larvae.[44–46] For example, Yang *et al*. developed an acoustic device with harmonic interdigital transducers (IDTs) to generate Rayleigh surface acoustic waves (SAWs) to enable the control of cell-cell distance and the manufacture of colloidal clusters with different configurations.[38] Collins *et al*. developed a SAW device to generate high-frequency two-dimensional (2D) standing SAWs to achieve single-cell patterning with one cell per acoustic potential well.[25] Huang *et al*. developed a SAW device that can be integrated with lithium-ion batteries to overcome the intrinsic limitations of fast charging by taking advantage of the SAW generated streaming. Riaud *et al*. developed swirling SAW devices to generate an acoustic vortex for selectively trapping of single micro-objects and translating the trapped objects along complex paths.[17]

Given the success of previous acoustofluidic devices, extensive studies are still needed to address their limitations and develop next-generation techniques with more functions. For example, in previous acoustofluidic devices, to independently generate and control acoustic waves from multiple transducers, they needed to use multiple function generator channels physically wired to the transducers.[25,47] Existing acoustofluidic devices cannot wirelessly

generate and control acoustic waves at different frequencies or propagating directions. On the other hand, in order to introduce on-demand liquid sample processing and micro/nano-object manipulation functions to wearable[48–50] and embeddable electronics[51–53] and sensing technologies,[54,55] wireless acoustofluidic chips are highly desired. However, few studies achieved wirelessly powered and controlled acoustofluidic chips, which can wirelessly activate key acoustofluidic functions such as generating acoustic streaming, concentrating particles, and arranging cells. These desired wireless acoustofluidic chips have great potential to facilitate the development of future wearable sensors with both wireless sensing and active liquid sample processing functions, future embedded electronics that can embedded in biomaterials to provide flow generation and acoustic stimulation functions, as well as future lab-on-a-chip technologies with wireless on-chip flow generation, fluid mixing, bioparticle separation, and bioparticle concentration functions. The wireless acoustofluidic chips also have great potential to be integrated with existing biomedical equipment to introduce new functions, for example, integrating them with cell culture chambers for cell arrangement, acoustic streaming-based flow control, and cell simulation in cell culture environments.

This study presents wireless frequency-multiplexed acoustofluidic devices, which can wirelessly generate megahertz traveling and standing acoustic waves and control the wave energy patterns for enabling multiple wirelessly activated and controlled acoustofluidic functions, such as arranging particles into different patterns, aligning cells, generating acoustic streaming, and concentrating in-droplet microparticles. To achieve these functions, particularly, our wireless acoustofluidic chips fuse mechanisms, including inductive coupling that has been used for WPT and near-field communication[56], frequency-multiplexing-based control of an array of IDTs with different resonance frequencies for generating and controlling multiple acoustic waves at different frequencies and propagating directions, as well as the resultant fluid streaming and applied forces on in-fluid micro/nano-objects. To develop wireless

acoustofluidic devices, we performed numerical and analytical simulations, as well as laser Doppler vibrometry-based characterization of the displacement fields of wirelessly generated acoustic waves, at multiple testing conditions with different distances between the WPT transmitter and receiver and different materials (*e.g.*, bone, tissue, and hand) inserted between them. Through a series of experiments, we demonstrated multiple critical functions of our wireless acoustofluidic devices, including (i) wirelessly sending power through different barriers (*e.g.*, bone, tissue, and hand) to multiple acoustic transducers to generate traveling and standing acoustic waves with different energy field distributions; (ii) wirelessly and independently controlling multiple IDTs and acoustic waves propagating in different directions based on the wireless frequency multiplexing mechanism; (iii) aligning nanoparticles and constructing lattice-like-patterns of nanoparticle clusters; (iv) arranging randomly distributed cells into multiple single-cell pearl chains in parallel; (v) generating streaming with a vortex-like flow field; and (vi) enriching in-droplet microparticles by gradually transporting microparticles to the droplet center and accumulating them. It is also worth noting that our demonstrations cover devices based on both low-frequency Lamb waves guided by the two parallel surfaces of a piezoelectric wafer, as well as high-frequency Rayleigh SAWs guided by one surface. This study contributes to acoustofluidic techniques by opening a paradigm of developing wireless Lamb wave and SAW-based acoustofluidic devices that can achieve key acoustofluidic functions such as arranging cells and micro/nanoparticles, generating acoustic streaming, and enriching in-droplet particles. Moreover, our approach can wirelessly transfer sufficient energy through interceding media (*e.g.*, bone, tissue, and hand) to piezoelectric chips to generate Lamb waves and SAWs and further enable various acoustofluidic functions. Our wireless approach breaks the limitations of previous wired devices and holds great potential for extending the functions and applications of acoustofluidic techniques. With the aforementioned

features, in the long run, we expect wireless acoustofluidics to lead to useful wearable and embeddable devices for engineering, veterinary, and biomedical applications.

2. Results and Discussion

2.1. Design and mechanism of a wireless acoustofluidic device

The wireless acoustofluidic device (see **Figure 1a** for a schematic) has three key modules, including (i) an acoustic chip with IDTs deposited on a $LiNbO_3$ piezoelectric wafer to generate acoustic waves for arranging micro/nano-objects and generating fluid streaming, (ii) a removable microfluidic chamber for loading liquids and micro/nano-objects to the acoustic wave generation region, as well as (iii) a customized WPT module, which can wirelessly send power and information from the WPT transmitter to the WPT receiver and then to the IDTs for generating and controlling acoustic waves. The wireless acoustofluidic device's working mechanism is illustrated in **Figure 1b**. The WPT transmitter is applied with an input voltage signal $V_T(t)=A_T e^{i(\omega t+\varphi)}$, where A_T, ω, and φ are the signal amplitude, angular frequency, and phase, respectively. Through inductive coupling,[57,58] both power and information of the input signal are wirelessly transmitted to the WPT receiver with the received voltage signal expressed as $V_R(t)=A_R e^{i(\omega t+\varphi+\Delta\varphi)}$, where A_R and $\Delta\varphi$ are the received signal's amplitude and phase shift. The voltage signal $V_R(t)$ is then applied to the IDTs on a piezoelectric wafer to generate acoustic waves propagating in counter directions. The interference of these acoustic waves further generates a standing acoustic wave field with nodes and anti-nodes. Thus, small objects (such as micro/nanoparticles and cells with positive acoustic contrast factors) preloaded in the microfluidic chamber are subjected to acoustic radiation forces and can be trapped in acoustic potential wells located at acoustic nodes.

To enhance the wireless acoustofluidic device's performance, such as the output/input voltage ratio A_R/A_T and acoustic wave displacements, we have optimized the WPT module so

that its electrical resonance frequency matches the IDT's resonance frequency f_{IDT}. **Figure 2a** shows an equivalent circuit diagram of a WPT module with a series-series compensation topology. The power emission side (**Figure 2a** left), connected to an alternating current power source (*e.g.*, a function generator), has a coil-based WPT transmitter with an inductance L_{T1} and a matching circuit with a capacitance C_{T1}. The power receiving side (**Figure 2a** right), connected to the IDTs, has a coil-based WPT receiver with an inductance L_{R1} and a matching circuit with a capacitance C_{R1}. To maximize the acoustic wave generation efficiency, we engineer the inductances and capacitances to satisfy the resonant condition $2\pi f_{\mathrm{IDT}} = 1/\sqrt{L_{T1}C_{T1}} = 1/\sqrt{L_{R1}C_{R1}}$ for matching the WPT module's peak frequency with the IDT's resonance frequency. Three-dimensional (3D) finite element simulations were performed to optimize the WPT module' design parameters such as the transmitter and receiver coils' diameters and numbers of turns. **Figure S1** shows our 3D simulation model considering a WPT transmitter coil with its matching circuit, a WPT receiver coil with its matching circuit, a domain with air surrounding the circuits, and an outer layer for minimizing boundary reflection. Our simulation result in the *x*-*z* plane (see **Figure 2b**) shows that a strong electric field can be wirelessly induced in the receiver coil with optimized parameters. More details of the WPT module's design with its optimized parameters can be found in the Experimental Section.

Based on the mechanism illustrated in **Figure 1b**, the wireless acoustofluidic device can be wirelessly powered and controlled to achieve different acoustofluidic functions such as micro/nanoparticle patterning, cell arrangement, acoustic streaming generation, as well as small object concentration, as illustrated in **Figure 1c-1f**. Moreover, with different materials (*e.g.*, bone and tissue) inserted between the WPT transmitter and receiver, as shown in **Figure 1a**, the wireless power transfer based on inductive coupling can still be achieved to enable those acoustofluidic functions. We have used a laser vibrometry-based sensing system to characterize the wireless acoustic wave generation performance by measuring the generated acoustic waves

at different wireless power transfer conditions. In addition, a series of acoustofluidic experiments were performed to demonstrate our wireless acoustofluidic devices. The results of these experiments and their related data analysis are given below.

2.2. Over-barrier wireless generation of acoustic waves

Following the design and fabrication of a wireless acoustofluidic device, we characterized the device's ability to wirelessly generate acoustic waves. We measured the WPT voltage ratio A_R/A_T and the nanoscale displacements of generated acoustic waves at different conditions, including different distances between the parallelly arranged transmitter and receiver coils, as well as different materials (*e.g.*, carapace, skull, swine tissue, and human hand) inserted between the transmitter and receiver coils (see **Figure 2c**). The experimental result (**Figure 2d**) shows that the ratio between receiver and transmitter voltages (*i.e.*, output/input voltage ratio A_R/A_T) gradually changes from 5 to 20 MHz. When the transmitter and receiver are close to each other (*i.e.,* 8 mm), the voltage ratio peaks near ~0.95 at 10.83 MHz. With the increase of the transmitter-receiver distance from 8 to 48 mm, the results show that the peak ratio gradually decreases to ~0.3 with a negligible frequency shift. Moreover, when different materials (*e.g.*, carapace, skull, swine tissue, and human hand) are inserted between the transmitter and receiver, our approach can maintain efficient power transfer to the acoustic device at its resonance frequency of 10.83 MHz, as shown in **Figure 2e**. Our measurements show that the voltage ratio negatively correlates to the transmitter-receiver distance due to reduced inductive coupling efficiency, and the insertion materials lead to slight offsets compared to the results measured in air. In addition, we also evaluated the power transfer efficiency by measuring S_{11} and S_{12} with a vector network analyzer (E5061B, Keysight, USA) and then calculating the efficiency with the relation $\eta=S_{12}/(1-S_{11})$[59]. The measured power transfer efficiencies were 91%, 57%, and 15% for transfer distances of 8 mm, 18 mm, and 28 mm, respectively.

Next, we used a customized scanning laser Doppler vibrometry setup to characterize the wirelessly generated acoustic waves, as illustrated in **Figure 3a** (see a photograph in **Figure S2**). In this setup, a function generator provides a voltage signal at the acoustic device's resonance frequency, and the excitation signal is sent to an IDT through the WPT module to generate traveling acoustic waves. On the other hand, a laser Doppler vibrometer, whose laser beam is perpendicular to the piezoelectric wafer and focused on the wafer's top surface, is adopted to measure the generated acoustic wave's out-of-plane displacement at the laser spot based on the Doppler effect.[60] By gradually changing the laser spot position along a serpentine path using a linear motion stage, the laser vibrometer can perform point-by-point acquisition of acoustic wave displacements at different locations. The combination of displacement waveforms acquired at all the scanning points provides the traveling acoustic wave's time-space wavefield $u(t, \mathbf{x})$ as a function versus time t and position $\mathbf{x}$. More details of the laser vibrometry approach can be found in the Experimental Section.

The acquired time-space wavefield in **Figure 3b** (also see **Movie S1**) clearly shows the propagation of a straight-wavefront acoustic wave with a wavelength of ~370 μm wirelessly generated by our device when the excitation frequency is 10.83 MHz, and the coil-to-coil distance is 1 mm. For further characterization, acoustic wave displacements are measured (see **Figure 3c**) at different voltages. It can be seen that the acoustic wave displacements gradually increase from 0 to ~1 nm, when the voltages measured at the IDT increase from 0 to 8 V. **Figure 3d** shows that the generated acoustic wave displacements gradually decrease with the increase of the coil-to-coil distance. In addition, for cases with different materials (such as carapace, skull, swine tissue, and human hand) inserted between the transmitter and receiver coils, the laser vibrometry results confirm the successful wireless generation of acoustic waves. This feature is critical to developing acoustofluidic chips that can be embedded in different materials and wirelessly activated for manipulating fluids and small objects.

2.3. Wireless frequency-multiplexed acoustic array

Various acoustofluidic devices leverage an array of acoustic transducers for generating acoustic waves propagating in different directions for transporting objects in different directions, as well as generating various acoustic energy patterns for constructing different cell/particle patterns. To wirelessly power and control an array of acoustic transducers, one approach is using multiple independent WPT modules and multiple waveform generation channels. This strategy significantly increases the system complexity and cost with the increase of the transducer number. Therefore, we have developed a wireless frequency-multiplexed acoustic array, which is less complex and more cost-effective.

As illustrated by the equivalent circuit diagram in Figure 4a, three IDTs (denoted as IDT_1 to IDT_3) with different pitches working at different resonance frequencies are interconnected to form a frequency-multiplexed acoustic array. When a signal carrying multiple frequency components, expressed as $s(t) = \sum_{n=1}^{3} A_n e^{i(\omega_n t + \varphi_n)}$, is sent to the frequency-multiplexed array, individual IDTs respond to different frequency components due to the IDTs' different resonance frequencies. Based on this mechanism, acoustic waves with different frequency-wavenumber components $\{(\omega_n, k_n)\}_{N=3}$ can be generated. Moreover, by changing the amplitude A_n and phase φ_n at an angular frequency ω_n, the acoustic wave generated at this frequency can be tuned. Furthermore, if the array has IDTs oriented in different directions, our approach can generate and control acoustic waves propagating in different directions by only using one AC input source. However, traditional approaches for generating and controlling acoustic waves propagating in N directions require the use of a total of N AC sources, with each source assigned to a specific direction[61–64].

For the success of the wireless frequency-multiplexed acoustic device, a WPT module working at multiple resonance frequencies matching the IDT frequencies is also critical. As

illustrated by the equivalent circuit diagram in **Figure 4a**, the multi-frequency WPT module has three sets of circuits, each using the series-series compensation topology similar to the design of the single-frequency WPT module illustrated in **Figure 2a**. These three circuits are optimized to work at different desired resonant frequencies, using the same approach for optimizing the single-frequency WPT module. To minimize the interference among the three sets of circuits, we used customized transformers with the same impedance ratio of 50 Ω/50 Ω for effective electromagnetic isolation. More details of the multi-frequency WPT module are given in the Experimental Section, and the electronics parameters for this module are in **Table S1**. We measured the output/input voltage ratios at different frequencies to characterize the multi-frequency WPT module. As shown in **Figure 4b**, the measured voltage ratio curve has three peaks at frequencies near the three IDTs' resonance frequencies f_1 = 10.8 MHz, f_2 = 13.4 MHz, and f_3 = 16.1 MHz, respectively, for exciting an array of three interconnected IDTs with different resonance frequencies. Then, the wireless frequency multiplexing-based generation of acoustic waves propagating in different directions was validated by measuring acoustic fields generated at different frequencies using a laser Doppler vibrometer, as well as constructing particle patterns with different orientations. The results of these experimental studies are given in the following subsection.

2.4. Multi-configuration patterning of nanoparticles

To demonstrate the wireless frequency-multiplexed acoustofluidic device, we measured the generated acoustic fields at different excitation frequencies and arranged 800 nm SiO_2 nanoparticles into different patterns. As illustrated in **Figure S3b** and **Figure 5a**, the acoustic array has four (M=4) IDT groups, and each group has three (N=3) frequency-multiplexed, interconnected IDTs working at different frequencies. **Figure S3d** shows a photo of the acoustic array. More details of the array design are given in the Experimental Section. When using the WPT module for wireless operation of the IDT groups 1 and 3, the acoustic fields (in **Figure**

5i to **5k**) measured by a laser Doppler vibrometer show standing acoustic waves with tilted node lines along 15, 45, and 75 deg directions at excitation frequencies of f_1 = 10.8 MHz, f_2 = 13.4 MHz, and f_3 = 16.1 MHz, respectively. The spacings between node lines are different due to the different wavelengths at the three frequencies. In addition, we tested a case with all four groups of IDTs connected to the WPT module. Two orthogonal pairs of IDTs can be activated by a signal with dual frequencies of f_1 = 10.80 and $f_1 + \Delta f$ = 10.83 MHz, as illustrated in **Figure 5d**. The slight frequency difference is related to the resonance frequency difference between IDTs with the same pitch but in different orientations, as the wave speed in an anisotropic piezoelectric wafer is direction-dependent. The acoustic intensity field (**Figure 5l**) measured by a laser Doppler vibrometer confirms the generation of a lattice-like standing acoustic field, having an array of potential valleys distributed on a 2D grid. Moreover, the acoustic fields (**Figure 5e-5h**) predicted by our analytical model (Section S1) agree with the experimental acoustic fields in **Figure 5i-5l**.

As our wireless frequency-multiplexed acoustic device can generate different standing acoustic wave patterns, it can apply acoustic radiation forces on small objects in the acoustic field to arrange their distributions. For demonstration, we used our device to pattern 800 nm-diameter SiO_2 nanoparticles. As shown in the captured brightfield microscopic images (**Figure 5m-o**), at different wireless excitation frequencies, SiO_2 nanoparticles can be arranged in parallel-line-like patterns with different line-to-line spacings and alignment orientations. When generating acoustic waves with a lattice-like intensity distribution using two orthogonal pairs of IDTs, nanoparticles are arranged in a 2D lattice-like pattern with an array of nanoparticle clusters shown in **Figure 5p**. The experiments above successfully demonstrate the ability of our wireless frequency-multiplexed acoustic array to generate acoustic waves propagating in different directions, and they also validate the ability to arrange small particles into different patterns.

2.5. Generating streaming, concentrating particles, and aligning cells

In addition to patterning particles using acoustic radiation force, we demonstrated other functions of our wireless acoustic device, such as wirelessly generating acoustic vortex streaming in a droplet, concentrating in-droplet microparticles, and aligning cells. First, an experiment was performed by adding a ~5 μL droplet to the traveling acoustic wave propagation region, as illustrated in **Figure 6a**. More details of the test procedure are in the Experimental Section. When the droplet is placed off the acoustic energy beam's center[65,66] (*e.g.*, close to the IDT side shown in **Figure 6a**), the traveling acoustic wave impinging on the droplet's side introduces angular momentum to the liquid, thus generating streaming with a vortex-like flow field. As confirmed by the recorded **Movie S2** and captured fluorescent images in **Figure 6b**, 5 μm green-fluorescent, tracing microparticles reveal a vortex-like streaming pattern after turning on the acoustic device. For this experiment, the peak power applied to the acoustic chip was 180 mW, and the acoustic chip's average temperature slightly increased by 0.2 °F with a local maximum increment of 0.6 °F (see **Figure S4**). If the acoustic chip is operated in a pulsed mode, such as being on for 6 sec and then off for 54 sec in every minute, the acoustic chip's average power can be reduced to 18 mW. Second, our experiment demonstrated the ability to concentrate in-droplet microparticles using the vortex streaming-induced drag force. As shown in the recorded **Movie S3** and captured fluorescent images in **Figure 6d**, 10 μm green-fluorescent polystyrene particles in a droplet are transported to the droplet center for accumulation after turning on acoustic waves. In these tests, 10 μm particles can be enriched, while 5 μm particles cannot, showing a size-dependent, in-droplet particle enrichment effect in agreement with previous studies on enriching in-droplet particles.[15,67,68] Multiple theoretical and experimental studies have found that the size threshold highly depends on frequency when using acoustic waves to separate and concentrate particles.[15, 65-70] Unlike previous studies using wired acoustic devices, this work demonstrates the ability to achieve in-droplet particle

enrichment using a wireless acoustic device, which is desirable for many wearable and implantable applications.[71,72] In addition to manipulating particles, we showed that our wireless acoustic device can manipulate bioparticles such as cells. The acquired microscopic image in **Figure 6f** shows that HepG2 cells can be arranged into multiple pearl chains parallel to each other after wirelessly generating standing acoustic waves using a device with a pair of IDTs. In the experiments above, acoustic waves generated by IDTs at 10.83 MHz actually are Lamb waves, as the $LiNbO_3$ substrate's thickness (500 μm) is not sufficiently larger than the wavelength (~370 μm).[2,3,73] To demonstrate wireless SAW acoustofluidics, we fabricated a device working at 40.0 MHz ensuring the generation of SAWs (wavelength ~100 μm) in a 500 μm-thick $LiNbO_3$ substrate. The result in **Figure 6h** shows that 800 nm-diameter SiO_2 nanoparticles are aligned by the wirelessly generated SAWs.

3. Discussion

This paper presents wireless acoustofluidic devices that can wirelessly generate acoustic waves carrying sufficient energy to enable multiple acoustofluidic functions such as arranging micro/nanoparticles in liquids, aligning cells, generating streaming to transporting particles and concentrating particles in a droplet. To enable these functions, notably, our device leverages an acoustic chip with multiple IDTs for acoustic wave generation, a removable microfluidic chamber for loading liquids and small objects, as well as an inductive coupling-based WPT module with rationally engineered electronics in a series-series compensation topology for wirelessly sending power and control signals to the acoustic chip. Moreover, by using a wireless frequency multiplexing mechanism, our approach can power and control an array of IDTs, thus generating various acoustic energy patterns such as parallel-line-like patterns in different orientations and lattice-like patterns of high-intensity spots to further arrange micro/nanoparticles into different distributions with acoustic radiation forces. On the one hand, this wireless frequency multiplexing mechanism takes advantage of a unique IDT rosette array

composed of interconnected IDTs with different resonance frequencies (*i.e.*, operation frequencies) and arranged in different orientations, for enabling the abilities to generate and control acoustic waves propagating in various directions using only one AC source. On the other hand, it adopts an extendable WPT module with multiple efficient power transfer frequencies that match the IDT resonance frequencies.

To characterize and demonstrate our wireless acoustofluidic device, we have measured the wirelessly generated acoustic wave displacement fields at different operation conditions and performed a series of acoustofluidic experiments to manipulate micro/nanoparticles and cells. The characterization results show that our device can wirelessly generate traveling acoustic waves with displacements (on the orders of 10^{-10} to 10^{-9} m) at conditions with different materials (*e.g.*, carapace, skull, swine tissue, and human hand) inserted between the WPT transmitter and receiver. The measured acoustic fields also confirm the ability to generate acoustic waves propagating in different directions and acoustic waves with a lattice-like energy pattern when using a wireless frequency-multiplexed acoustic device with interconnected IDTs working at different frequencies. The acoustofluidic experiments validate multiple device functions such as constructing cell pearl chains that are parallel to each other, arranging nanoparticles into different patterns (*e.g.*, parallel-line-like and lattice-like patterns), generating acoustic streaming with a vortex-like flow field, as well as concentrating microparticles in a droplet by transporting in-droplet particles to the droplet center and gradually accumulating them. Note that our devices with Y128-cut $LiNbO_3$ wafers have low efficiencies in generating waves not propagating along the X-direction; and we expect that using other cuts (*e.g.*, 152° Y-rotated $LiNbO_3$), which preserve high piezoelectric coupling efficiencies in multiple directions,[66,74] will improve the performance of the IDT rosette array.

In future research, we will replace the copper wire coils, which are used for inductive coupling in this study, with electrodes directly patterned on the acoustic substrate, as this change

can benefit the device miniaturization. We will also replace the $LiNbO_3$ piezoelectric plates in our current wireless acoustic devices with flexible piezoelectric materials such as films coated with piezoelectric materials (*e.g.*, aluminum nitride). We expect this change to push wireless acoustofluidics toward achieving wearable or embeddable acoustofluidic devices. The integration of acoustofluidic devices with wearable sensors may lead to devices with both liquid sample processing and sensing functions. In addition, we plan to enable other wireless acoustofluidic functions such as fluid mixing, bioparticle separation, cell lysis, changing particle alignment orientations and spacings, as well as translating a particle along designed complex paths. We expect the paradigm in this research to inspire researchers working on acoustofluidics, lab-on-a-chip devices, as well as wearable and embeddable electronics, for advancing the development of future wearable sensors with active liquid sample processing functions, lab-on-a-chip devices with embeddable wireless on-chip flow generators, as well as implantable chips with both biofluid flow generation and acoustic stimulation abilities.

4. Experimental Section

Design and fabrication of acoustofluidic chips

Schematics and photos of our acoustofluidic chips are given in **Figure S3**. The frequency-multiplexed acoustofluidic device consists of four (M=4) groups of IDTs, and each group has three (N=3) frequency-multiplexed IDTs that are designed with different pitches for different operation frequencies (f_1 = 10.8 MHz, f_2 = 13.4 MHz, and f_3 = 16.1 MHz). The n^{th} IDT in the m^{th} group is denoted as $IDT_{m,n}$. The workflow for fabricating IDTs on a $LiNbO_3$ wafer is illustrated in **Figure S5**. First, a photoresist layer is coated on a 500 μm-thick, Y128-cut $LiNbO_3$ wafer (double-side polished). Second, using photolithography and chemical development, the designed IDT patterns on a photomask can be transferred to the wafer. Third, e-beam evaporation is used to deposit a 10 nm-thick Chromium (Cr) layer and then a 90 nm-thick gold (Au) layer, followed by a lift-off process to obtain the desired IDTs. These steps allow a

frequency-multiplexed array of IDTs working at different frequencies to be fabricated on a $LiNbO_3$ chip. To perform acoustofluidic experiments, we attached a disposable microfluidic chamber on top of the acoustic substrate. This chamber is composed of a bottom layer (~100 μm thick) manufactured by a stereolithography 3D printer (Form3, Formlabs) and a glass coverslip (~100 μm thick) as the ceiling.

Design of a single-frequency WPT module

The WPT module with a single operation frequency of 10.83 MHz was designed and manufactured for the acoustic device with a pair of IDTs having a resonance frequency f_{IDT} of 10.83 MHz. **Figure 2a** shows an equivalent circuit diagram of the single-frequency WPT module. The power emission side has a coil inductor (inner diameter 33 mm, 5 turns) made of a 16-gauge silicone tinned copper wire, and the coil's inductance L_{T1} is 2.73 μH, measured by a vector network analyzer (E5061B, Keysight). The power receiving side has a coil inductor (inner diameter 13 mm, 11 turns), which is made of a 0.3 mm-diameter copper wire and has an inductance L_{R1} of 8.16 μH. The WPT transmitter and receiver should have the same resonance frequency to match the IDT's resonance frequency for maximized wireless power transfer efficiency through inductive coupling. For a series-series compensation topology, matching circuits for the WPT transmitter and receiver should have capacitances C_{T1} = 79.1 pF and C_{R1} = 26.5 pF, respectively, to satisfy the relation $2\pi f_{\mathrm{IDT}} = 1/\sqrt{L_{T1}C_{T1}} = 1/\sqrt{L_{R1}C_{R1}}$. In addition, we fabricated WPT circuits working at 40.0 MHz for the wireless SAW acoustofluidic device. The WPT transmitter's coil inductor has an inner diameter of 35 mm and 4 turns of 16-gauge silicone tinned copper wire. This coil's inductance is 5.3 μH, and its matching capacitance is 3.0 pF. The WPT receiver's coil, with an inner diameter of 23 mm and 12 turns, is made of a 0.3 mm-diameter copper wire. As this coil's inductance is 4.8 μH, its matching capacitance is 3.3 pF to achieve optimal wireless energy transfer at 40.0 MHz.

Design of a multi-frequency WPT module

To power and control a frequency-multiplexed array of IDTs with different resonance frequencies, we designed a WPT module having three peak frequencies near the IDT array's resonance frequencies f_1 =10.8 MHz, f_2 = 13.4 MHz, and f_3 = 16.1 MHz. As illustrated in **Figure 4a**, the WPT module comprises three sets of circuits optimized to efficiently transmit power at resonant frequencies f_1, f_2, and f_3, respectively. Each set of circuits uses the series-series compensation topology and is optimized using the same approach for optimizing the single-frequency WPT module. **Table S1** gives the determined electric parameters for the three sets of circuits. In addition, to minimize the interaction among the three sets of circuits, customized transformers with the same impedance ratio of 50 Ω/50 Ω are used to isolate them, as illustrated by the equivalent circuit diagram in **Figure 4a**. This isolation approach also allows for parallelly extending the circuit for transferring more than three frequency components. When extending the circuit, the operation frequencies should be carefully selected to avoid harmonic frequency matching, for minimizing electromagnetic interference among different operation frequencies.

Finite element simulation

To optimize the WPT module' design parameters, finite element simulations were performed in COMSOL Multiphysics. **Figure S1** shows a 3D schematic of the simulation model, containing a WPT transmitter with a matching circuit, a WPT receiver with a matching circuit, a domain Ω_1 with air, and a thin layer Ω_2 that is set to the "perfect electric conductor" condition for minimizing the boundary reflection. To simulate both the electric field and magnetic flux, the physics module, "electromagnetic waves" of COMSOL Multiphysics, is used to establish the finite element model. After simulation at a frequency of 10.83 MHz, matching the experimental frequency, we extracted the simulated electric field and magnetic flux in plane $\sum_1$ illustrated in **Figure S1,** and plotted the results in **Figure 2b**.

Laser vibrometry-based acoustic wave characterization

To characterize the performance of our wireless acoustic device, the laser vibrometry-based acoustic field measurement was performed. As illustrated by the experimental setup in **Figure S2**, a function generator (DG1022, Rigol) was employed to send an excitation signal to the WPT transmitter. A laser Doppler vibrometer (VFX-1-130, Polytec Inc.) was used to acquire the generated acoustic wave displacement. Particularly, the laser beam was perpendicular to the $LiNbO_3$ substrate, and the laser spot was focused on the substrate's top surface, in order to measure the out-of-plane displacement component based on the Doppler effect. The output voltage signals from the vibrometer's decoder were recorded by an oscilloscope (TDS 2014C, Tektronix), and the measured voltage signals were further converted to displacement waveforms by using the vibrometer's displacement decoder information (10 nm/V). In order to acquire a time-space wavefield of acoustic waves, the laser head is installed on a 3-DoF linear motion stage to move the laser position with a step size of 0.05 mm for point-by-point measurements. By combining the waveforms acquired at all scanning points on a 2D grid within the desired acoustic wave measurement region (5 × 5 mm), a time-space wavefield $u(t, \mathbf{x})$ containing the information of the generated acoustic waves can be obtained. To increase the signal-to-noise ratio, we acquired signals eight times at each measurement point and then averaged them. The collected raw data were post-processed using the Fourier transform to evaluate the acoustic wave signal's frequency component and visualize the acoustic field at the desired frequency.

Preparation of cell and particle solutions

Human hepatocellular carcinoma (HepG2) cells were used for the cell patterning experiment. They were maintained in DMEM medium (Gibco, Life Technologies) supplemented with 10% fetal bovine serum (Gibco, Life Technologies), penicillin (50 units·mL^{-1}; Sigma-Aldrich), and streptomycin (50 μg·mL^{-1}; Sigma-Aldrich) in an incubator (CCL-B, ESCO Technologies Pty

Ltd.) at 37 ℃ with a carbon dioxide (CO_2) level of 5%. Before each experiment, HepG2 cells were harvested and resuspended in fresh DMEM medium to an approximate concentration of 1.0×10^6 mL^{-1}. For patterning nanoparticles, 800 nm-diameter SiO_2 nanoparticles were suspended in deionized water to a concentration of ~1.5×10^6 mL^{-1}. For visualizing acoustic streaming, 5 μm-diameter green-fluorescent polystyrene beads (Cospheric LLC) suspended in deionized water were used. For demonstrating acoustofluidic particle concentration, 10 μm-diameter green-fluorescent polystyrene particles (Cospheric LLC) in deionized water were used.

Acoustofluidic experiments

We performed a series of acoustofluidic experiments including nanoparticle patterning, cell arrangement, acoustic streaming generation, and particle concentration. Input signals for the WPT transmitter were generated by a function generator (AFG3052C, Tektronix Inc.). The signal obtained by the WPT receiver was monitored by an oscilloscope (2190E, B&K Precision Corporation). The wirelessly transmitted voltage signal is used to excite the IDTs on the $LiNbO_3$ substrate to generate acoustic waves, which can further arrange nanoparticles and cells, generate an acoustic streaming vortex, and concentrate small objects. For nanoparticle patterning, a solution with 800 nm-diameter SiO_2 nanoparticles was loaded into a microfluidic chamber attached to the piezoelectric substrate. For cell arrangement, a solution with HepG2 cells was loaded into the microfluidic chamber. To demonstrate acoustic streaming, a 5 μL droplet containing 5 μm polystyrene particles was added to the piezoelectric substrate. To demonstrate in-droplet particle concentration, a 5 μL droplet containing 10 μm polystyrene particles was added to the acoustic wave propagation region. The fabricated wireless acoustofluidic device was placed on the stage of an inverted optical microscope (TE2000-U, Nikon) for monitoring the cell/particle manipulation process.

Supporting Information

Supporting Information is available from the Wiley Online Library or from the author.

Acknowledgements

The authors acknowledge the financial support from the National Institute of General Medical Sciences of the National Institutes of Health (7R01GM144417), National Science Foundation (CMMI 2243771 and CMMI 2340016), and Nuclear Energy University Programs (DE-NE0009187). We also acknowledge the support from the Virginia Tech Advanced Research Computing Services.

Conflict of Interest

The authors declare no conflict of interest.

Data Availability Statement

The data that support the findings of this study are available from the corresponding authors upon reasonable request.

Received: ((will be filled in by the editorial staff))
Revised: ((will be filled in by the editorial staff))
Published online: ((will be filled in by the editorial staff))

References

[1] A. Ozcelik, J. Rufo, F. Guo, Y. Gu, P. Li, J. Lata, T. J. Huang, *Nat. Methods* **2018**, *15*, 1021.
[2] J. Friend, L. Y. Yeo, *Rev. Mod. Phys.* **2011**, *83*, 647.
[3] J. Rufo, F. Cai, J. Friend, M. Wiklund, T. J. Huang, *Nat. Rev. Methods Primer* **2022**, *2*, 1.
[4] L. Moroni, J. A. Burdick, C. Highley, S. J. Lee, Y. Morimoto, S. Takeuchi, J. J. Yoo, *Nat. Rev. Mater.* **2018**, *3*, 21.
[5] J. Wu, *J. Acoust. Soc. Am.* **1991**, *89*, 2140.
[6] J. P. K. Armstrong, J. L. Puetzer, A. Serio, A. G. Guex, M. Kapnisi, A. Breant, Y. Zong, V. Assal, S. C. Skaalure, O. King, T. Murty, C. Meinert, A. C. Franklin, P. G. Bassindale, M. K. Nichols, C. M. Terracciano, D. W. Hutmacher, B. W. Drinkwater, T. J. Klein, A. W. Perriman, M. M. Stevens, *Adv. Mater.* **2018**, *30*, 1.
[7] G. Bao, S. Suresh, *Nat. Mater.* **2003**, *2*, 715.

[8] G. M. Whitesides, *Nature* **2006**, *442*, 368.
[9] M. Scott, A. W. Bangel III, X. Song, Y. Xie, *Adv. Mater. Technol.* **2023**, *8*, 2300424.
[10] A. Marzo, B. W. Drinkwater, *Proc. Natl. Acad. Sci.* **2019**, *116*, 84.
[11] R. Hirayama, D. Martinez Plasencia, N. Masuda, S. Subramanian, *Nature* **2019**, *575*, 320.
[12] A. Ozcelik, Z. Aslan, *Microfluid. Nanofluidics* **2021**, *25*, 5.
[13] M. Stringer, Z. Zeng, X. Zhang, Y. Chai, W. Li, J. Zhang, H. Ong, D. Liang, J. Dong, Y. Li, Y. Fu, X. Yang, *Appl. Phys. Rev.* **2023**, *10*, 011315.
[14] Y. Wang, Q. Zhang, R. Tao, J. Xie, P. Canyelles-Pericas, H. Torun, J. Reboud, G. McHale, L. E. Dodd, X. Yang, J. Luo, Q. Wu, Y. Fu, *ACS Appl. Mater. Interfaces* **2021**, *13*, 16978.
[15] G. Destgeer, H. Cho, B. Hang Ha, J. Ho Jung, J. Park, H. Jin Sung, *Lab. Chip* **2016**, *16*, 660.
[16] N. Zhang, A. Horesh, J. Friend, *Adv. Sci.* **2021**, *8*, 2100408.
[17] A. Riaud, J. L. Thomas, E. Charron, A. Bussonnière, O. Bou Matar, M. Baudoin, *Phys. Rev. Appl.* **2015**, *4*.
[18] M. Aghaamoo, Y.-H. Chen, X. Li, N. Garg, R. Jiang, J. T.-H. Yun, A. P. Lee, *Adv. Sci.* **2022**, *9*, 2102021.
[19] M. Baudoin, J.-C. Gerbedoen, A. Riaud, O. B. Matar, N. Smagin, J.-L. Thomas, *Sci. Adv.* **2019**, *5*, eaav1967.
[20] N. Garg, T. M. Westerhof, V. Liu, R. Liu, E. L. Nelson, A. P. Lee, *Microsyst. Nanoeng.* **2018**, *4*, 1.
[21] Y. Yang, Y. Yang, D. Liu, Y. Wang, M. Lu, Q. Zhang, J. Huang, Y. Li, T. Ma, F. Yan, H. Zheng, *Nat. Commun.* **2023**, *14*, 3297.
[22] R. Habibi, V. He, S. Ghavamian, A. de Marco, T.-H. Lee, M.-I. Aguilar, D. Zhu, R. Lim, A. Neild, *Lab. Chip* **2020**, *20*, 3633.
[23] D. J. Collins, C. Devendran, Z. Ma, J. W. Ng, A. Neild, Y. Ai, *Sci. Adv.* **2016**, *2*, 2.
[24] C. Bouyer, P. Chen, S. Güven, T. T. Demirtaş, T. J. F. Nieland, F. Padilla, U. Demirci, *Adv. Mater.* **2016**, *28*, 161.
[25] D. J. Collins, B. Morahan, J. Garcia-Bustos, C. Doerig, M. Plebanski, A. Neild, *Nat. Commun.* **2015**, *6*, 1.
[26] M. G. Kim, J. Park, H. G. Lim, S. Yoon, C. Lee, J. H. Chang, K. K. Shung, *Sci. Rep.* **2017**, *7*, 14092.
[27] M. Kim, P. V. Bayly, J. Mark Meacham, *Lab. Chip* **2021**, *21*, 521.
[28] J. Zhang, J. H. Hartman, C. Chen, S. Yang, Q. Li, Z. Tian, P.-H. Huang, L. Wang, J. N. Meyer, T. Jun Huang, *Lab. Chip* **2020**, *20*, 1729.
[29] M. Sundvik, H. J. Nieminen, A. Salmi, P. Panula, E. Hæggström, *Sci. Rep.* **2015**, *5*.
[30] B. W. Drinkwater, *Lab. Chip* **2016**, *16*, 2360.
[31] D. Ahmed, T. Baasch, N. Blondel, N. Läubli, J. Dual, B. J. Nelson, *Nat. Commun.* **2017**, *8*, 770.
[32] T. Franke, A. R. Abate, D. A. Weitz, A. Wixforth, *Lab. Chip* **2009**, *9*, 2625.
[33] Y. Hu, Y. Wang, M. Zhang, C. Gao, P. Zhao, S. Zhang, Z. Zan, D. Li, Z. Fan, *Small Sci. n/a*, 2300146.
[34] M. Antfolk, C. Magnusson, P. Augustsson, H. Lilja, T. Laurell, *Anal. Chem.* **2015**, *87*, 9322.
[35] M. Dao, S. Suresh, T. J. Huang, P. Li, Z. Mao, Z. Peng, L. Zhou, Y. Chen, P. H. Huang, C. I. Truica, J. J. Drabick, W. S. El-Deiry, *Proc. Natl. Acad. Sci. U. S. A.* **2015**, *112*, 4970.
[36] K. Olofsson, B. Hammarström, M. Wiklund, *Lab. Chip* **2020**, *20*, 1981.
[37] B. Chen, Y. Wu, Z. Ao, H. Cai, A. Nunez, Y. Liu, J. Foley, K. Nephew, X. Lu, F. Guo, *Lab. Chip* **2019**, *19*, 1755.
[38] S. Yang, Z. Tian, Z. Wang, J. Rufo, P. Li, J. Mai, J. Xia, H. Bachman, P. H. Huang, M. Wu, C. Chen, L. P. Lee, T. J. Huang, *Nat. Mater.* **2022**, *21*, 540.
[39] M. Tayebi, D. Yang, D. J. Collins, Y. Ai, *Nano Lett.* **2021**, *21*, 6835.

[40] M. Wu, Y. Ouyang, Z. Wang, R. Zhang, P. H. Huang, C. Chen, H. Li, P. Li, D. Quinn, M. Dao, S. Suresh, Y. Sadovsky, T. J. Huang, *Proc. Natl. Acad. Sci. U. S. A.* **2017**, *114*, 10584.
[41] J. Zhu, Q. Zhang, F. Liang, Y. Feng, W. Wang, *J. Micromechanics Microengineering* **2021**, *31*, 124004.
[42] N. Sridhar, A. Kefin Fajrial, R. L. Doser, F. J. Hoerndli, X. Ding, *Lab. Chip* **2022**, *22*, 4882.
[43] J. Bhadra, N. Sridhar, A. K. Fajrial, N. Hammond, D. Xue, X. Ding, *Sci. Adv.* **2023**, *9*, eadf5056.
[44] C. Chen, Y. Gu, J. Philippe, P. Zhang, H. Bachman, J. Zhang, J. Mai, J. Rufo, J. F. Rawls, E. E. Davis, N. Katsanis, T. J. Huang, *Nat. Commun.* **2021**, *12*.
[45] V. M. Jooss, J. S. Bolten, J. Huwyler, D. Ahmed, *Sci. Adv.* **2022**, *8*, eabm2785.
[46] Z. Zhang, Y. Cao, S. Caviglia, P. Agrawal, S. C. F. Neuhauss, D. Ahmed, *Lab. Chip* **2024**, *24*, 764.
[47] L. Ren, S. Yang, P. Zhang, Z. Qu, Z. Mao, P.-H. Huang, Y. Chen, M. Wu, L. Wang, P. Li, T. J. Huang, *Small* **2018**, *14*, 1801996.
[48] L. Yin, S. S. Sandhu, R. Liu, M. I. Khan, C. Wicker, V. Garcia-Gradilla, J. Zhou, A.-Y. Chang, S. Wu, J.-M. Moon, C. Chen, S. Ding, J. Wang, *Adv. Energy Mater.* **2023**, *13*, 2203418.
[49] H. Hu, H. Huang, M. Li, X. Gao, L. Yin, R. Qi, R. S. Wu, X. Chen, Y. Ma, K. Shi, C. Li, T. M. Maus, B. Huang, C. Lu, M. Lin, S. Zhou, Z. Lou, Y. Gu, Y. Chen, Y. Lei, X. Wang, R. Wang, W. Yue, X. Yang, Y. Bian, J. Mu, G. Park, S. Xiang, S. Cai, P. W. Corey, J. Wang, S. Xu, *Nature* **2023**, *613*, 667.
[50] C. Wang, E. Shirzaei Sani, W. Gao, *Adv. Funct. Mater.* **2022**, *32*, 2111022.
[51] C. M. Boutry, L. Beker, Y. Kaizawa, C. Vassos, H. Tran, A. C. Hinckley, R. Pfattner, S. Niu, J. Li, J. Claverie, Z. Wang, J. Chang, P. M. Fox, Z. Bao, *Nat. Biomed. Eng.* **2019**, *3*, 47.
[52] C. M. Boutry, A. Nguyen, Q. O. Lawal, A. Chortos, S. Rondeau-Gagné, Z. Bao, *Adv. Mater.* **2015**, *27*, 6954.
[53] J. A. Chiong, H. Tran, Y. Lin, Y. Zheng, Z. Bao, *Adv. Sci.* **2021**, *8*, 2101233.
[54] Y. Xu, E. De la Paz, A. Paul, K. Mahato, J. R. Sempionatto, N. Tostado, M. Lee, G. Hota, M. Lin, A. Uppal, W. Chen, S. Dua, L. Yin, B. L. Wuerstle, S. Deiss, P. Mercier, S. Xu, J. Wang, G. Cauwenberghs, *Nat. Biomed. Eng.* **2023**, *7*, 1307.
[55] Y. Yu, J. Li, S. A. Solomon, J. Min, J. Tu, W. Guo, C. Xu, Y. Song, W. Gao, *Sci. Robot.* **2022**, *7*, eabn0495.
[56] C. Degen, *EURASIP J. Wirel. Commun. Netw.* **2021**, *2021*, 121.
[57] A. Kurs, A. Karalis, R. Moffatt, J. D. Joannopoulos, P. Fisher, M. Soljačić, *Science* **2007**, *317*, 83.
[58] M. Song, P. Jayathurathnage, E. Zanganeh, M. Krasikova, P. Smirnov, P. Belov, P. Kapitanova, C. Simovski, S. Tretyakov, A. Krasnok, *Nat. Electron.* **2021**, *4*, 707.
[59] A. Bharadwaj, A. Sharma, C. C. Reddy, *IEEE Trans. Instrum. Meas.* **2022**, *71*, 1.
[60] P. Kudela, M. Radzieński, W. Ostachowicz, *Mech. Syst. Signal Process.* **2015**, *50–51*, 456.
[61] A. Riaud, M. Baudoin, J.-L. Thomas, O. Bou Matar, *IEEE Trans. Ultrason. Ferroelectr. Freq. Control* **2016**, *63*, 1601.
[62] A. Riaud, J.-L. Thomas, M. Baudoin, O. Bou Matar, *Phys. Rev. E* **2015**, *92*, 063201.
[63] F. Guo, Z. Mao, Y. Chen, Z. Xie, J. P. Lata, P. Li, L. Ren, J. Liu, J. Yang, M. Dao, S. Suresh, T. J. Huang, *Proc. Natl. Acad. Sci. U. S. A.* **2016**, *113*, 1522.
[64] X. Ding, S.-C. S. Lin, B. Kiraly, H. Yue, S. Li, I.-K. Chiang, J. Shi, S. J. Benkovic, T. J. Huang, *PANS* **2012**, 109 (28) 11105-11109.
[65] R. Shilton, M. K. Tan, L. Y. Yeo, J. R. Friend, *J. Appl. Phys.* **2008**, *104*, 014910.
[66] N. Zhang, J. P. Zuniga-Hertz, E. Y. Zhang, T. Gopesh, M. J. Fannon, J. Wang, Y. Wen, H. H. Patel, J. Friend, *Lab. Chip* **2021**, *21*, 904.

[67] P. Dumčius, R. Mikhaylov, X. Zhang, M. Bareford, M. Stringer, R. Errington, C. Sun, E. Gonzalez, T. Krukovski, J. M. Falcon-Perez, D. Liang, Y.-Q. Fu, A. Clayton, X. Yang, *Small* **2023**, *19*, 2300390.
[68] J. Rich, B. Cole, T. Li, B. Lu, H. Fu, B. N. Smith, J. Xia, S. Yang, R. Zhong, J. L. Doherty, K. Kaneko, H. Suzuki, Z. Tian, A. D. Franklin, T. J. Huang, *Microsyst. Nanoeng.* **2024**, *10*, 1.
[69] R. Barnkob, P. Augustsson, T. Laurell, H. Bruus, *Phys. Rev. E* **2012**, *86*, 056307.
[70] D. J. Collins, Z. Ma, Y. Ai, *Anal. Chem.* **2016**, *88*, 5513.
[71] D. K. Piech, B. C. Johnson, K. Shen, M. M. Ghanbari, K. Y. Li, R. M. Neely, J. E. Kay, J. M. Carmena, M. M. Maharbiz, R. Muller, *Nat. Biomed. Eng.* **2020**, *4*, 207.
[72] J. C. Chen, P. Kan, Z. Yu, F. Alrashdan, R. Garcia, A. Singer, C. S. E. Lai, B. Avants, S. Crosby, Z. Li, B. Wang, M. M. Felicella, A. Robledo, A. V. Peterchev, S. M. Goetz, J. D. Hartgerink, S. A. Sheth, K. Yang, J. T. Robinson, *Nat. Biomed. Eng.* **2022**, *6*, 706.
[73] A. Huang, W. Connacher, M. Stambaugh, N. Zhang, S. Zhang, J. Mei, A. Jain, S. Alluri, V. Leung, A. E. Rajapaksa, J. Friend, *Lab. Chip* **2021**, *21*, 1352.
[74] N. Zhang, J. Mei, T. Gopesh, J. Friend, *IEEE Trans. Ultrason. Ferroelectr. Freq. Control* **2020**, *67*, 2176.

Figures

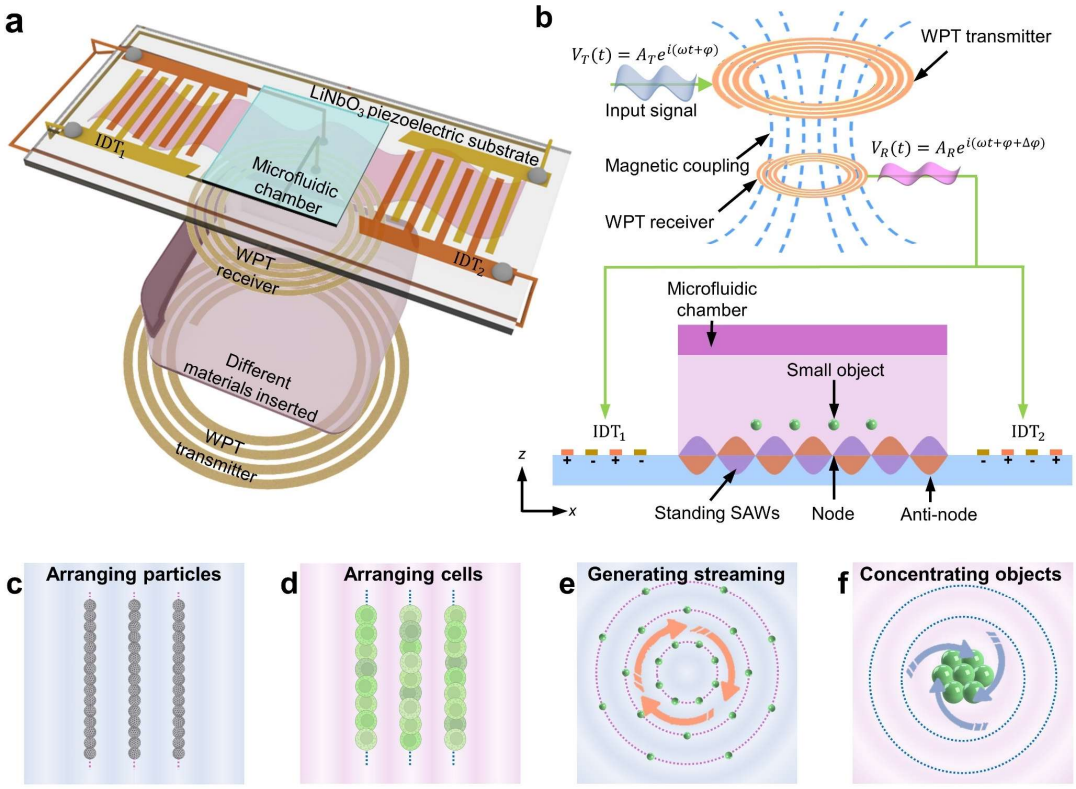

Figure 1. Mechanism and applications of the wireless acoustofluidic device. (a) Schematic of the wireless acoustofluidic device. Key components include an acoustic chip with a pair of IDTs, a microfluidic chamber for cell/particle manipulation, a WPT transmitter, and a WPT receiver. **(b)** Operation mechanism, starting from the excitation signal $V_T(t)$ (with amplitude A_T and angular frequency ω) applied to the WPT transmitter, induced voltage signal $V_R(t) = A_R e^{(i\omega t+\Delta\varphi)}$ (with amplitude A_R and phase shift $\Delta\varphi$) in the WPT receiver via inductive coupling and subsequent generation of on-chip standing acoustic waves for arranging small particles in a microfluidic chamber. **(c-f)** Acoustofluidic multifunctionalities. Wireless acoustofluidic devices can realize **(c)** particle arrangement, **(d)** cell arrangement, **(e)** acoustic vortex streaming generation, and **(f)** concentration of small objects.

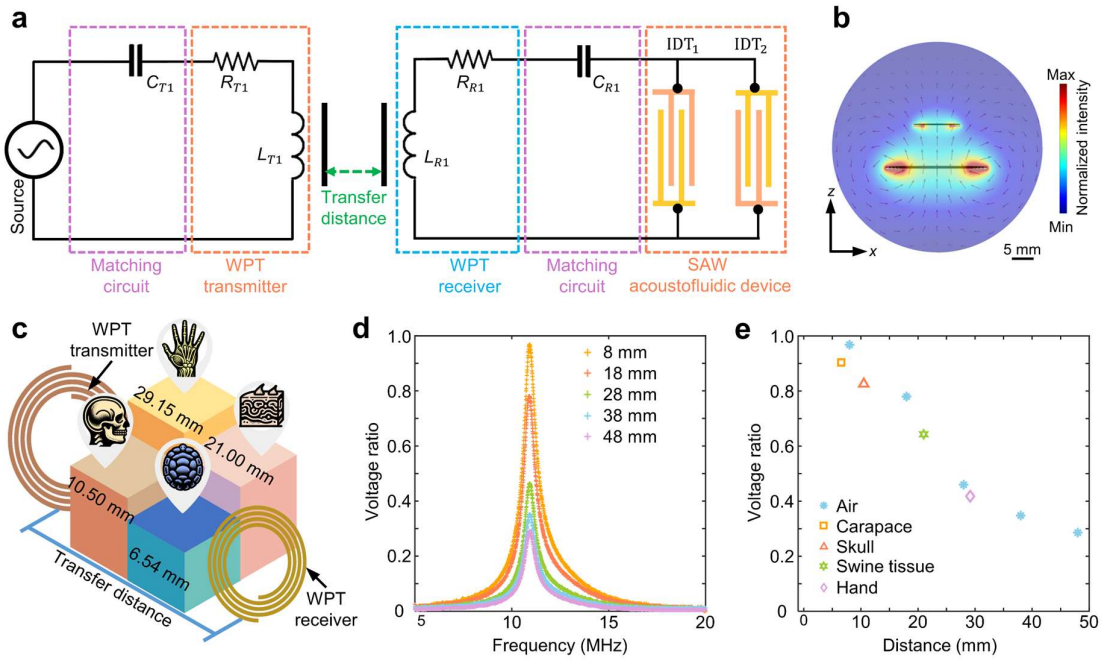

Figure 2. **Wireless single-frequency acoustofluidic device: mechanism, simulation, and characterizations**. **(a)** Equivalent circuit diagram, modeling the electrical behavior of the system for optimization and analysis. The power emission side of the WPT module has a power source (*e.g.*, a function generator), a matching circuit, and a WPT transmitter based on a coil inductor. The power receiving side has a WPT receiver based on a coil inductor, a matching circuit, and an acoustofluidic device with multiple IDTs. The matching circuits can adjust the impedance parameters to enhance the power transfer efficiency. **(b)** The finite element modeling (details in Figure S1) simulates the electric field (color) and magnetic flux (arrow) in the *x*-*z* plane, illustrating the electromagnetic interactions within the system. **(c)** Schematic of different materials, including carapace, skull, swine tissue, and hand, inserted between the WPT transmitter and receiver with different distances of 6.54, 10.50, 21.00, and 29.15 mm, respectively. **(d)** Measured WPT voltage ratios (A_R/A_T) with different transmitter-receiver distances. The graph shows a sharp peak at 10.83 MHz to match the IDT's resonant frequency. **(e)** Comparison of measured voltage ratios (A_R/A_T) at the resonant frequency of 10.83 MHz for different insertion materials and transmitter-receiver distances.

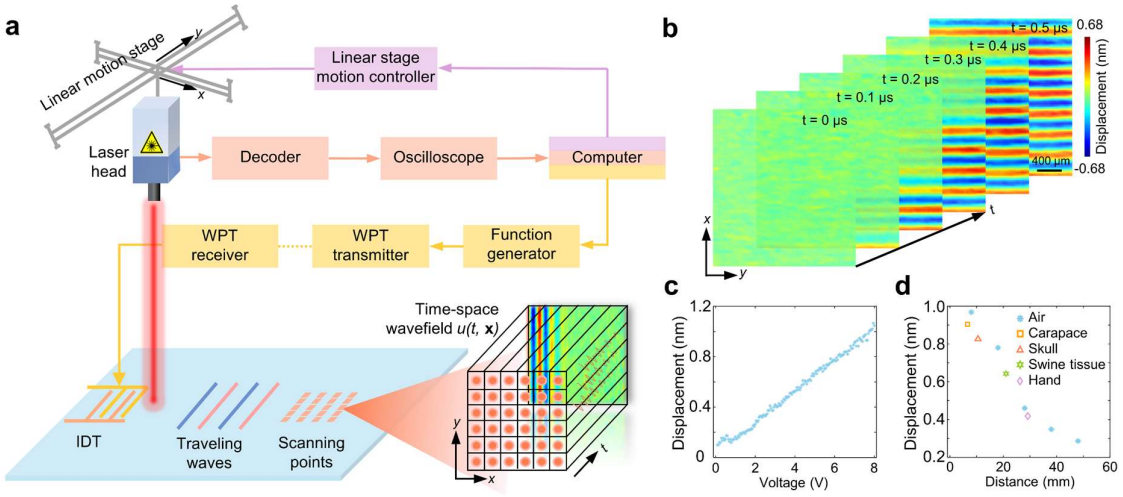

Figure 3. **Laser vibrometry characterization of a wireless acoustofluidic device**. **(a)** Laser vibrometry setup. Schematic illustrates how the laser vibrometry system acquires a time-space wavefield $u(t, \mathbf{x})$ of the wirelessly generated on-chip acoustic waves. The wireless device generates traveling acoustic waves, and a laser vibrometer installed on a linear motion stage acquires acoustic wave signals at different locations point-by-point. Combining the waveforms from all the sensing positions yields a time-space wave field $u(t, \mathbf{x})$. (A photo of this system can be found in Figure S2.) **(b)** Measured time-resolved wavefield distributions of traveling acoustic waves generated by our wireless acoustofluidic chip at a frequency of 10.83 MHz. **(c)** Measured acoustic wave displacements at different voltages applied to the WPT receiver. The distance between the WPT transmitter and receiver is set to 10 mm without an insertion material. **(d)** Comparison of measured acoustic wave displacements at the resonance frequency of 10.83 MHz for cases with different insertion materials and transmitter-receiver distances.

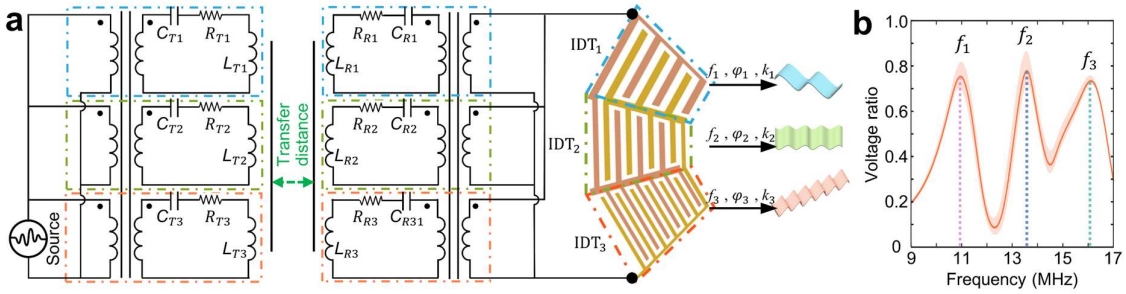

Figure 4. Frequency-multiplexed wireless acoustofluidic device. **(a)** Equivalent circuit diagram for frequency multiplexing. This design incorporates a WPT transmitter and a WPT receiver, each comprising three LC resonant circuits and matching with frequency-multiplexed IDTs working at different resonant frequencies (f_1, f_2, and f_3). The WPT module uses small transformers to minimize the coupling between different LC resonant circuits. With this design, the WPT module can have three resonance peaks. Moreover, an input signal with three frequency components f_1, f_2, and f_3 generated by the source (*e.g.*, a functional generator) can be wirelessly transmitted to a group of three IDTs, which can further generate acoustic waves with wavenumbers k_1, k_2, and k_3 and phases φ_1, φ_2, and φ_3, respectively. **(b)** Measured voltage ratio (A_R/A_T) spectra with three transmission peaks at frequencies close to the resonance frequencies of the three IDTs. The curve's shadow reveals the measurement error.

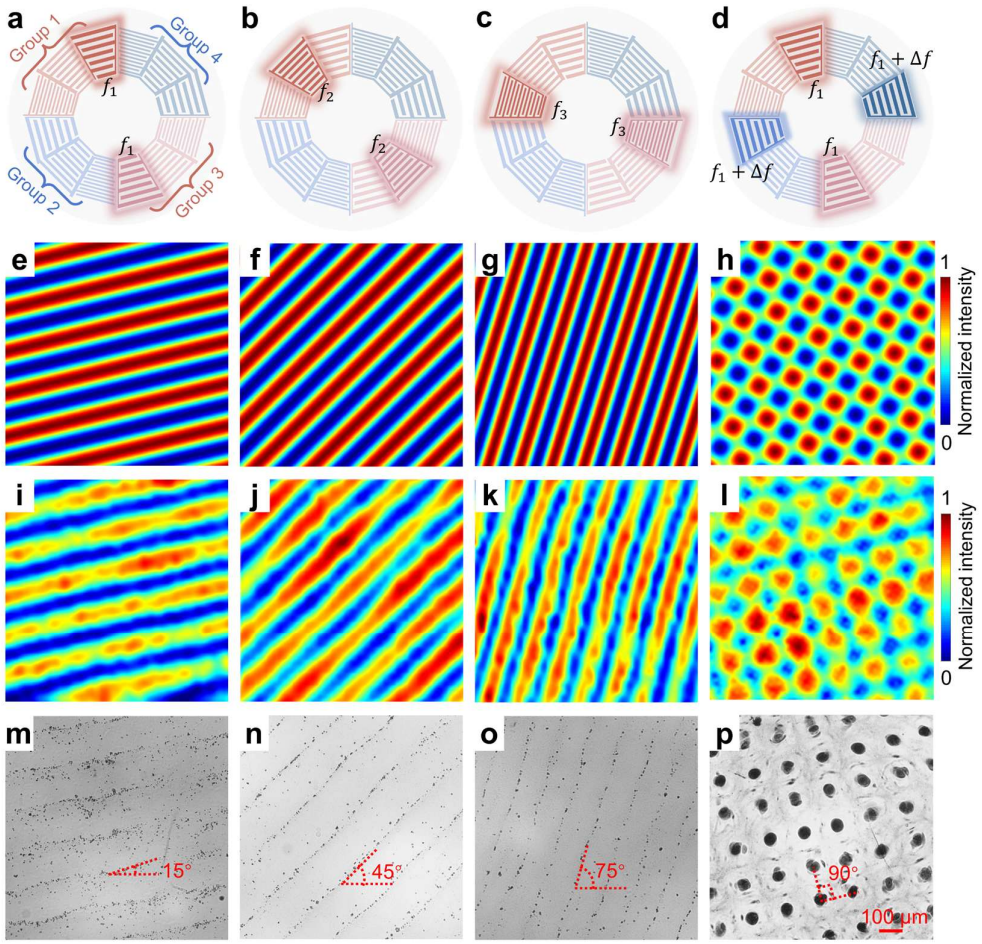

Figure 5. Frequency-multiplexed wireless acoustofluidic nanoparticle patterning. **(a-d)** Schematics for illustrating the activated pairs of IDTs in the frequency-multiplexed acoustofluidic device. **(e-h)** Simulated wave intensity field distributions using an analytical model in Supplementary Section S1. **(i-l)** Measured wave intensity field distributions using a laser vibrometry system. **(m-p)** Brightfield microscopy images showing different patterns of 800 nm-diameter SiO_2 nanoparticles constructed by the generated standing acoustic waves (scale bar: 100 μm). The first, second, and third rows are for cases when the device is excited at f_1 =10.8 MHz, f_2 = 13.4 MHz, and f_3 = 16.1 MHz, receptively. The fourth row is for the case when two orthogonally arranged pairs of IDTs are excited at frequencies of 10.80 MHz and 10.83 MHz, respectively.

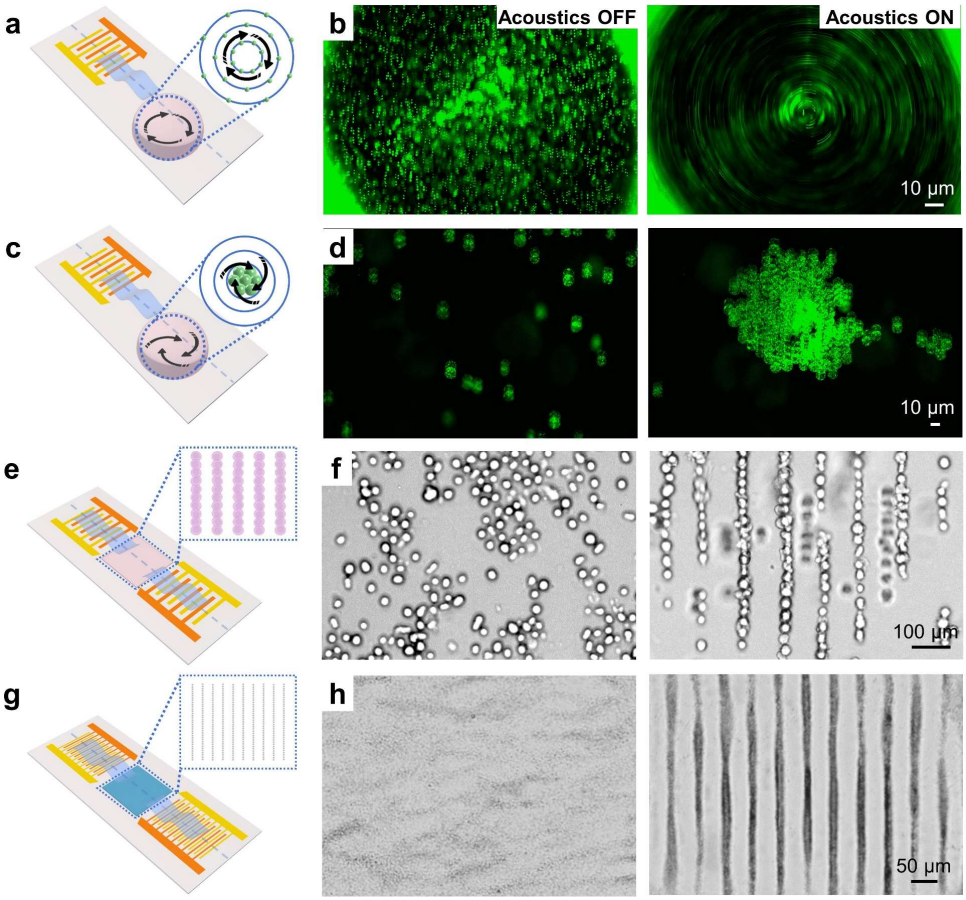

Figure 6. Experimental results showing the key functions of wireless acoustofluidic devices including acoustic streaming, microparticle concentration, cell alignment, and particle alignment. (a, b) A schematic of the test setup and acquired fluorescence microscopic images for demonstrating acoustic streaming. The images show 10.83 MHz traveling acoustic wave-induced vortex-like streaming in a droplet with 5 μm polystyrene particles on the piezoelectric substrate. **(c, d)** A schematic of the test setup and acquired fluorescence microscopic images for demonstrating microparticle concentration. The images show 10.83 MHz traveling acoustic wave-induced concentration of 10 μm polystyrene particles in a droplet on the piezoelectric substrate. **(e, f)** A schematic of the test setup and acquired brightfield microscopic images for demonstrating cell alignment. The images show HepG2 cells aligned by 10.83 MHz standing acoustic waves. **(g, h)** A schematic of the test setup and acquired brightfield microscopic images for particle alignment. The images show 800 nm SiO_2 nanoparticles aligned by standing SAWs at 40.0 MHz. In Figures **b**, **d**, **f**, and **h**, the left and right columns give images obtained at conditions without and with acoustic waves.